


 Cite this: *RSC Adv.*, 2024, **14**, 21982

A first-principles prediction of novel Janus ZrGeZ_3H ($\text{Z} = \text{N, P, and As}$) monolayers: Raman active modes, piezoelectric responses, electronic properties, and carrier mobility

 Tuan V. Vu, ^{ab} Vo T. T. Vi, ^c Nguyen T. Hiep, ^{*de} Khanh V. Hoang,^f A. I. Kartamyshev,^{ab} Huynh V. Phuc ^{*g} and Nguyen N. Hieu ^{de}

In this article, an attempt is made to explore new materials for applications in piezoelectric and electronic devices. Based on density functional theory calculation, we construct three Janus ZrGeZ_3H ($\text{Z} = \text{N, P, and As}$) monolayers and study their stability, piezoelectricity, Raman response, and carrier mobility. The results from phonon dispersion spectra, *ab initio* molecular dynamics simulation, and elastic coefficients confirm the structural, thermal, and mechanical stability of these proposed structures. The ZrGeZ_3H monolayers are indirect band gap semiconductors with favourable band gap energy of 1.15 and 1.00 eV for the ZrGeP_3H and ZrGeAs_3H , respectively, from Heyd–Scuseria–Ernzerhof functional method. It is found that the Janus ZrGeZ_3H monolayers possess both in-plane and out-of-plane piezoelectric coefficients, revealing that they are potential piezoelectric candidates. In addition, the carrier mobilities of electrons and holes along transport directions are anisotropic. Notably, the ZrGeP_3H and ZrGeAs_3H monolayers have high electron mobility of 3639.20 and 3408.37 $\text{cm}^2 \text{V}^{-1} \text{s}^{-1}$, respectively. Our findings suggest the potential application of the Janus ZrGeZ_3H monolayers in the piezoelectric and electronic fields.

Received 5th June 2024

Accepted 6th July 2024

DOI: 10.1039/d4ra04107k

rsc.li/rsc-advances

1 Introduction

It is well known that fossil fuels such as oil and coal are non-renewable energy sources. In addition, using these fossil fuels induces high emissions of CO_2 and other pollutants resulting in severe problems of global warming and environmental pollution. Therefore, many efforts have been made to find new alternative energy sources. Piezoelectric technology is an attractive approach for renewable and environmentally friendly energies. Based on the piezoelectric effect, piezoelectric materials can generate electricity from mechanical energy or *vice versa*. The piezoelectric properties of materials are closely related to the symmetry of crystal structure.^{1–3} A piezoelectric

material needs to have a non-centrosymmetric structure. Thus, studies on materials that have non-centrosymmetric structures for piezoelectric response are necessary.

The Janus two-dimensional (2D) materials have been explored with various unique features such as electronic,^{4,5} optical,⁶ catalytic,^{7,8} thermoelectric,⁹ piezoelectric,^{10,11} properties due to their intrinsic asymmetry structures.^{12,13} Especially, experimental and theoretical works have demonstrated the application prospects of 2D materials in the piezoelectric field. For instance, Duerloo *et al.* discovered the intrinsic piezoelectricity in 2D transition metal dichalcogenides based on the density functional theory investigations. The high in-plane piezoelectric coefficients of 9.13 pm V^{-1} were obtained for MoTe_2 material.¹⁴ The GaSe and SnSe monolayers were also revealed to be piezoelectric materials with high piezoelectric coefficients.^{15,16} Interestingly, the Janus structures with the broken mirror symmetry caused out-of-plane polarization dipole, resulting in an additional out-of-plane piezoelectricity. Guo and co-workers constructed Janus structures of group III monochalcogenides by first-principles calculations. They found that these group III Janus chalcogenides exhibited piezoelectricity with both in-plane piezoelectric coefficients (up to 8.47 pm V^{-1}) and extra out-of-plane piezoelectric coefficient of $0.07\text{--}0.46 \text{ pm V}^{-1}$.¹⁷ Some other 2D Janus structures also possessed additional out-of-plane piezoelectric effect such as XTeI ($\text{X} = \text{Sb/}$

^aLaboratory for Computational Physics, Institute for Computational Science and Artificial Intelligence, Van Lang University, Ho Chi Minh City, Vietnam. E-mail: tuan.vu@vlu.edu.vn

^bFaculty of Mechanical – Electrical and Computer Engineering, School of Technology, Van Lang University, Ho Chi Minh City, Vietnam

^cFaculty of Basic Sciences, University of Medicine and Pharmacy, Hue University, Hue 530000, Vietnam

^dInstitute of Research and Development, Duy Tan University, Da Nang 550000, Vietnam. E-mail: nguyenthithiep2@duytan.edu.vn

^eFaculty of Natural Sciences, Duy Tan University, Da Nang 550000, Vietnam

^fPhenikaa Institute for Advanced Study (PIAS), Phenikaa University, Hanoi 12116, Vietnam

^gDivision of Physics, School of Education, Dong Thap University, Cao Lanh 870000, Vietnam. E-mail: hvphuc@dthu.edu.vn



Bi,¹⁸ MoSTe,¹⁹ MoSO,²⁰ γ -Sn₂XY (X and Y are the chalcogen atoms),²¹ and BMX₂ (M = Ga or In; X = S/Se).²²

The recent experimental discovery of 2D MoSi₂N₄ and WSi₂N₄ monolayers has promoted great interest in 2D materials which composed from seven atoms.²³ Consequently, a family of 2D materials with the general formula MA₂Z₄ has been theoretically reported.²⁴ The MA₂Z₄ family exhibits high structural stability and outstanding physical properties. Some Janus materials have been derived from the MA₂Z₄ family, such as MSiGeN₄,²⁵ MGeSiP₄,²⁶ and XM₂N₂.²⁷ These Janus compounds also exhibit piezoelectric properties, making them suitable for applications in piezoelectric devices.

Inspired by the need for new materials for renewable energy and the research on Janus MA₂N₄-based materials, in this article, we design 2D Janus ZrGeZ₃H (Z = N, P, and As) monolayers, and predict their stabilities, structural and electronic characteristics, Raman response, and carrier mobility by using the first-principles calculations. At the same time, we also investigate the piezoelectric properties in these monolayers.

2 Computational details

Based on density functional theory (DFT), to investigate the electronic structures of material we used the projector augmented wave method as implemented in the Vienna *ab initio* simulation package (VASP).^{28,29} We employed the GGA parameterized by Perdew, Burke, and Ernzerhof (PBE) to study the exchange–correlation potential.³⁰ To gain more accurate results for band structure, we used the hybrid functional suggested by Heyd, Scuseria and Ernzerhof (HSE06).³¹ The phonon calculations were performed by the VASP+PHONOPY code using the density functional perturbation theory (DFPT).³² We set the convergence threshold for force and energy as 10^{-3} eV Å⁻¹ and 10^{-6} eV, respectively. We selected a $12 \times 12 \times 1$ *k*-point grid to sample the first Brillouin zone (BZ). The energy cut-off for a plane wave basis was 650 eV. We set up a 20 Å vacuum to eliminate interlayer interactions. The interactions of van der Waals (vdW) between the layers were described by the semi-empirical DFT-D3 method.³³ The Raman activity was tested by calculating the macroscopic dielectric tensor.³⁴ Within DFPT, we computed the elastic tensors and piezoelectric stress tensors. *Ab initio* molecular dynamics (AIMD) calculation was used³⁵ to test the thermodynamic stability of Janus systems. We corrected our computation with the dipole adjustment to correct for the dipole moment inherent in the asymmetric material. The carrier mobility in the materials was computed using the deformation potential approach.³⁶

3 Results and discussion

3.1 Structure, stability, and Raman activity

Fig. 1 illustrates the crystal structure with the unit cell of Janus ZrGeZ₃H monolayers in equilibrium. The 2D ZrGeZ₃H crystal structures are built from the ZrGe₂Z₄ symmetric monolayers by simultaneously removing the GeZ atomic layer and replacing it with an H atomic layer. The 2D Janus ZrGeZ₃H monolayers have a vertically asymmetric structure concerning the central atomic

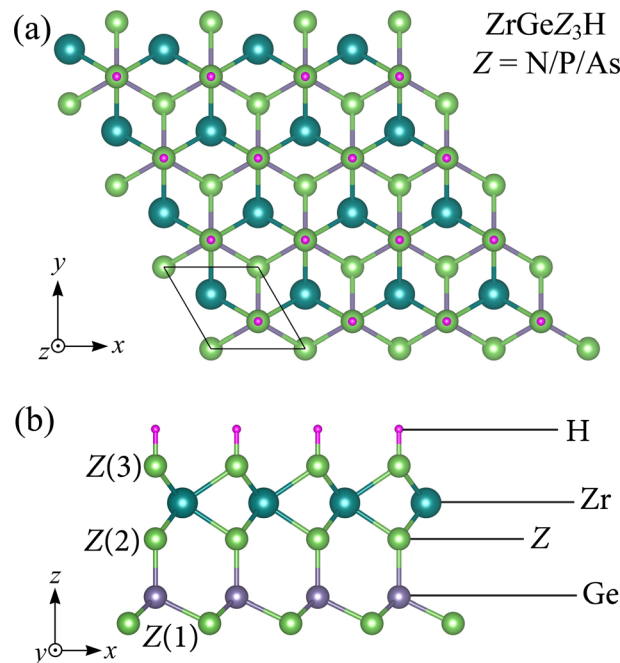


Fig. 1 (a) Top and (b) side views of the ZrGeZ₃H (Z = N, P, and As) crystal structures.

layer Zr. The unit cell of ZrGeZ₃H contains six atoms as shown in Fig. 1. We calculate the structural parameters of the Janus ZrGeZ₃H monolayers and list them in Table 1. The results show that the values of lattice constant, bond length as well as thickness of the monolayer gradually increase with the increasing atomic number of Z element. The ZrGeN₃H, ZrGeP₃H, and ZrGeAs₃H monolayers have lattice constant (*a*) of 3.18, 3.76, and 3.90 Å, respectively. These achieved values are comparable to those of the reported ZrGe₂Z₄ monolayer.²⁴

After calculating the structural parameters of the 2D ZrGeZ₃H crystals, we examine their structural stability to explore their feasibility under conventional conditions. Fig. 2 depicts phonon dispersion spectra and AIMD simulations of all three Janus ZrGeZ₃H monolayers. As we can observe, there are 18 vibrational branches because of six atoms in the unit cell. More importantly, the absence of imaginary frequencies in the BZ implies that the Janus ZrGeZ₃H exhibits high kinetic stability. The obtained AIMD calculations for 10 ps at room temperature show that the total energies of the monolayers fluctuate only in a very small range throughout the simulation, revealing the predicted thermodynamic stability of the ZrGeZ₃H monolayers. Besides, the bond strength between atoms in

Table 1 Lattice constant *a* (Å), thickness *h* (Å) bond length *d* (Å), and cohesive energy *E*_{coh} (eV per atom) of Janus ZrGeZ₃H monolayers

	<i>a</i>	<i>h</i>	<i>d</i> ₁	<i>d</i> ₂	<i>d</i> ₃	<i>d</i> ₄	<i>d</i> ₅	<i>E</i> _{coh}
ZrGeN ₃ H	3.18	5.90	2.20	2.21	1.88	1.92	1.03	-7.23
ZrGeP ₃ H	3.76	7.68	2.63	2.61	2.31	2.39	1.42	-5.52
ZrGeAs ₃ H	3.90	8.08	2.72	2.71	2.41	2.50	1.53	-5.08



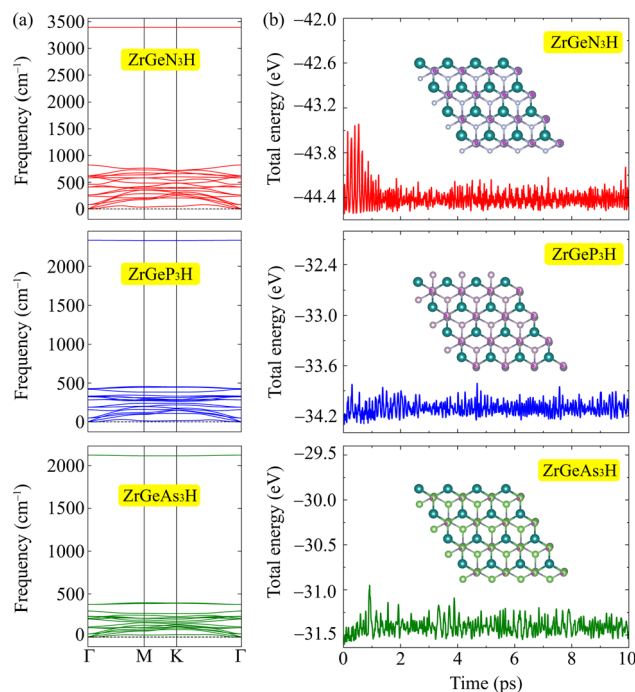


Fig. 2 (a) The calculated phonon spectra and (b) AIMD results for the total energy to simulation time at 300 K of ZrGeZ₃H monolayers.

structure is investigated based on the cohesive energy as follows:

$$E_{\text{coh}} = \frac{(E_{\text{Zr}} + E_{\text{Ge}} + 3E_{\text{Z}} + E_{\text{H}}) - E_{\text{tot}}}{N_{\text{tot}}}, \quad (1)$$

Here, N_{tot} is the total number of atoms in the unit cell ($N = 6$). E_{Zr} , E_{Ge} , E_{H} , and E_{Z} are the energies of single elements Zr, Ge, H, and Z, respectively. E_{tot} represents the total energy of the Janus system.

The obtained values of cohesive energy (E_{coh}) are listed in Table 1. All three ZrGeZ₃H monolayers exhibit negative E_{coh} and the ZrGeN₃H system has the highest cohesive energy value. This indicates that the ZrGeN₃H is the most energetically stable compared to the other two monolayers. It is known that N has a smaller atomic radius than P and As, thus the bond length in the ZrGeN₃H monolayer is smaller than that in the ZrGeP₃H and ZrGeAs₃H, leading to the highest interatomic bond strength in the ZrGeZ₃H among the three investigated structures.

Additionally, we analyze the structural phases of Janus ZrGeZ₃H systems using Raman spectra. An approach that is frequently used to examine the physical properties of materials with crystallographic symmetry is Raman spectroscopy analysis. Raman spectroscopy can be used to determine several properties of the materials, including their stoichiometry, lattice symmetry, electronic structure, and structural phase. Fig. 3 displays the computed Raman spectra of the ZrGeZ₃H monolayers. We observe that all three monolayers exhibit relatively intense and sharp Raman peaks. The ZrGeN₃H shows the high-intensity Raman peaks at 822, 612, and 462 cm⁻¹. Notably, the most intense peak of the ZrGeZ₃H shifts from 822 cm⁻¹ for the ZrGeN₃H to lower frequency of 322 cm⁻¹ for the ZrGeP₃H and

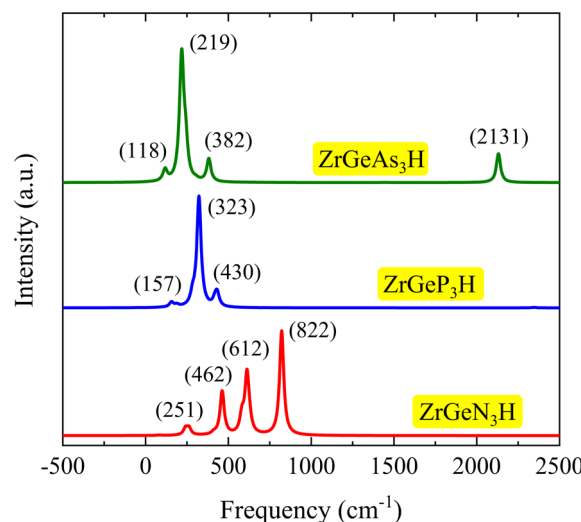


Fig. 3 Raman spectra of ZrGeZ₃H monolayers. The intensity with respect to the frequency.

219 cm⁻¹ for the ZrGeAs₃H monolayer. This shift of Raman peaks relates to the increase in atomic mass of the Z atom.

3.2 Electronic properties

Fig. 4 illustrates the electronic energy band structure of the three ZrGeZ₃H monolayers. Herein, we simultaneously use the PBE functional and the HSE06 hybrid functional to evaluate the electronic states of all compounds. Except for the band gap value, both HSE06 and PBE methods give similar results in terms of energy band profile as well as the positions of the conduction band minimum (CBM) and valence band maximum (VBM). All three ZrGeZ₃H compounds are indirect semiconductors, but the ZrGeN₃H monolayer has a much wider band gap than the other two monolayers. The PBE band gap value gradually decreases from 1.99 to 0.35 eV as Z element goes from N to As. Besides, the band gap value calculated from the HSE06 is larger than that calculated from the PBE method. However, the decreasing tendency of the band gap when Z changes from N to As is still preserved. The HSE06 band gap energy reaches the maximum value of 3.28 eV for the ZrGeN₃H monolayer. Table 2 tabulates the calculated results for the band gap energies of the three Janus ZrGeZ₃H monolayers.

To gain a deeper understanding of the formation of energy band structure from atomic orbitals, we carry out the projected band using the PBE method. Fig. 5 depicts the projected bands of the three Janus ZrGeZ₃H configurations at the PBE level. We can see that the d orbital of the Zr element has a major contribution to the construction of the conduction band, and the p orbital of the Z element participates mainly in the formation of the valence band. Besides, the VBM is also made up from the d orbital of the Zr atom.

Further, we investigate the work function at the surfaces of the Janus ZrGeZ₃H monolayers by evaluating the electrostatic potential. Since the two crystal surfaces are formed by different atoms, the crystal structure is asymmetric with respect to the central atomic layer. Therefore, an intrinsic electric field



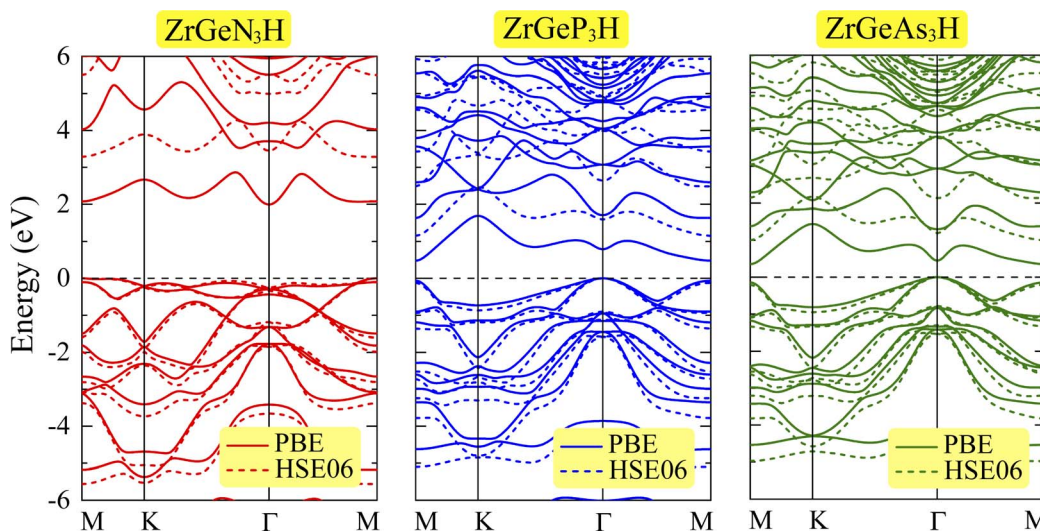


Fig. 4 Electronic band structure of ZrGeZ_3H monolayers at PBE/HSE06 levels. The dashed horizontal line at zero is the Fermi level.

Table 2 The elastic coefficients C_{ij} , Young's modulus Y_{2D} and Poisson's ratio ν and piezoelectric coefficients e_{11} , e_{31} , d_{11} , and d_{31} of the proposed ZrGeZ_3H materials

	C_{11} (N m^{-1})	C_{12} (N m^{-1})	C_{66} (N m^{-1})	Y_{2D} (N m^{-1})	ν	$e_{11} 10^{-10} \text{ C m}^{-1}$	$e_{31} 10^{-10} \text{ C m}^{-1}$	d_{11} (pm V^{-1})	d_{31} (pm V^{-1})
ZrGeN_3H	254.41	96.40	79.00	217.88	0.38	2.17	0.22	1.38	0.06
ZrGeP_3H	104.12	35.12	34.50	92.26	0.34	-1.88	-0.06	-2.72	-0.04
ZrGeAs_3H	90.46	34.11	28.18	77.60	0.38	-2.50	-0.19	-4.44	-0.15

appears in the perpendicular direction to the planar plane of the material. The magnitude of electric field intensity depends on the electronegativity difference between the different atoms on the two sides of the structure. Therefore, we need to use dipole correction for the electrostatic potential calculation. Fig. 6 depicts the obtained electrostatic potential of the Janus ZrGeZ_3H compounds. It is easy to observe that the electrostatic potential possesses an asymmetric shape due to the asymmetric structure of Janus compounds. The work function depends on the Fermi level and the vacuum level by $\varphi = E_v - E_f$. This quantity represents the minimum energy that an electron needs to attain to escape from the surface of the crystal. Table 3 shows the calculated work function and vacuum level difference data with the dipole correction. The vacuum level difference between the H and N faces is much higher than between the H and P faces or between the H and As faces. In addition, electrons escape more easily from the H surface than from the Z surface because of the lower work function at the H surface.

3.3 Mechanical properties and piezoelectricity

In this section, we discover the mechanical properties and piezoelectricity of the ZrGeZ_3H monolayers. Firstly, we report the mechanical properties by calculating the elastic constants, Young's modulus, and Poisson's ratio. For the 2D systems with a hexagonal structure, the elastic constants that need to be calculated are C_{11} and C_{12} because the other quantities C_{22} and C_{66} are determined through C_{11} and C_{12} as $C_{22} = C_{11}$ and $C_{66} =$

$(C_{11} - C_{12})/2$. Table 2 lists the obtained values of the elastic constants, which satisfy the Born–Huang criterion for mechanical stability. Thus, ZrGeZ_3H monolayers are predicted to be mechanically stable systems.

To evaluate the flexibility of the Janus ZrGeZ_3H configurations, we calculated their Young's modulus Y_{2D} , which is defined as follows:

$$Y_{2D} = \frac{C_{11}^2 - C_{12}^2}{C_{11}}. \quad (2)$$

The value of Y_{2D} changes from 77.60 to 217.88 N m^{-1} when the group V element goes from As to N. In other words, when Z element is N, the corresponding monolayer ZrGeN_3H has the highest in-plane stiffness. It can be due to the smallest lattice constant and highest cohesive energy in the ZrGeN_3H monolayer. The Y_{2D} value of ZrGeN_3H is lower than graphene³⁷ but higher than MoS_2 .³⁸

Then, we determine Poisson's ratio of the materials, which represents the mechanical response to the applied stress. Poisson's ratio is calculated from the obtained elastic constants by the following formula:

$$\nu = \frac{C_{12}}{C_{11}}. \quad (3)$$

The calculated ν values for all predicted monolayers are also isotropic due to their geometric structure. Table 2 reveals that the ZrGeP_3H monolayer has the smallest ν , while the remaining systems have a higher ν of 0.38. These obtained values of Poisson's



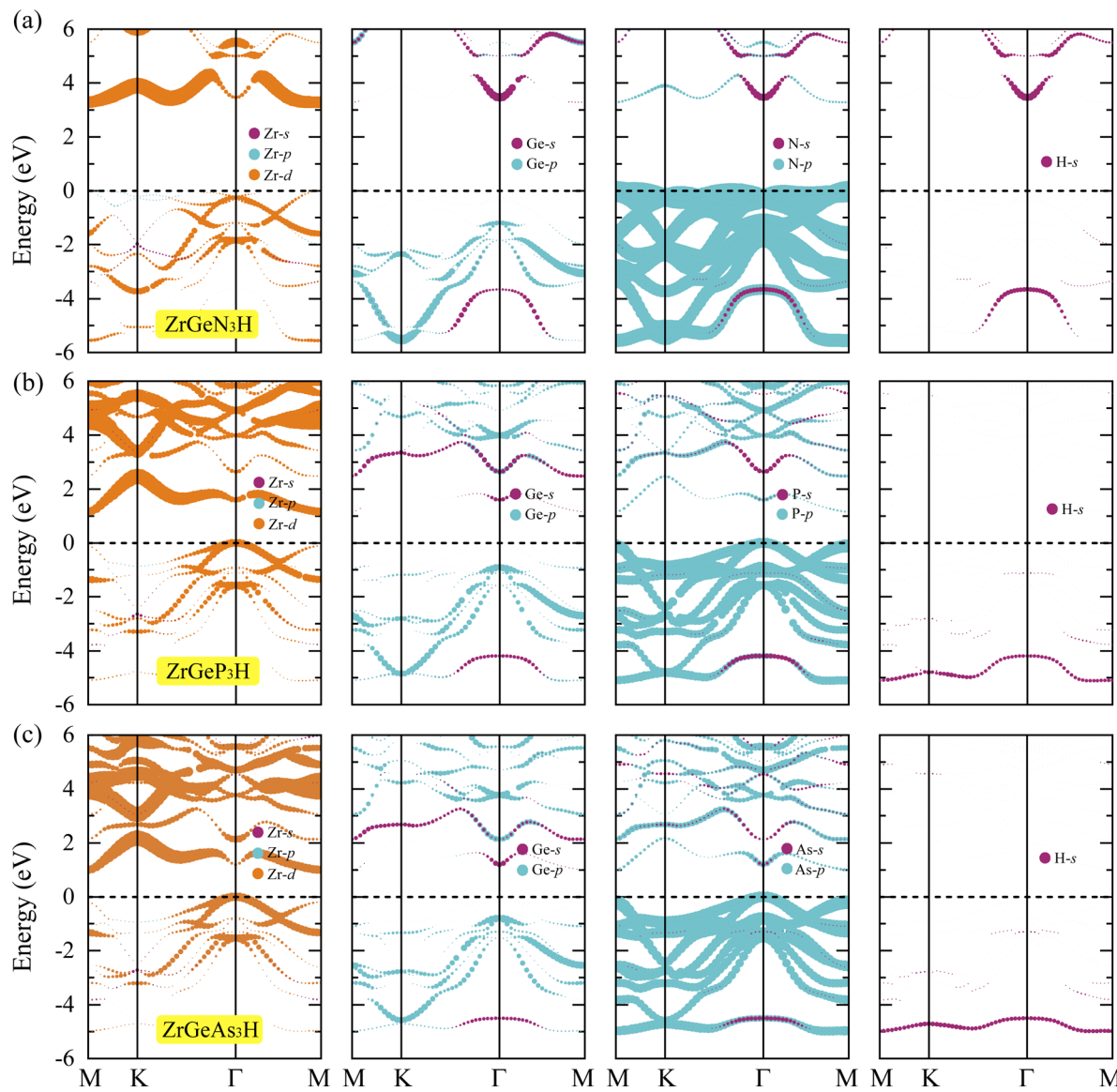


Fig. 5 Projected band at the PBE level of (a) ZrGeN₃H, (b) ZrGeP₃H, and (c) ZrGeAs₃H monolayers.

ratio are higher than graphene³⁷ and MoS₂,³⁸ implying that our considered monolayers are more sensitive to uniaxial strain.

Piezoelectricity is a special effect of the materials; it exhibits efficient performance of converting mechanical energy into electrical energy or *vice versa*. The piezoelectric response of the material is closely related to the symmetry of the crystal. Specifically, piezoelectric materials should be non-centrosymmetric. Our monolayers belong to the point symmetry group *P3m1*, which are Janus structures lacking centrosymmetry. Therefore, we can expect that these monolayers exhibit piezoelectric properties.

It is well-known that uniaxial deformation causes polarization in the crystal structure of materials. It is the basis for investigating the linear piezoelectric coefficient *via* piezoelectric stress/strain (e_{ijk}/d_{ijk}) tensor. The piezoelectric stress/strain tensor is a third-order tensor, which is defined *via* the surface polarization (P) and strain/stress ($\varepsilon_{jk}/\partial\sigma_{jk}$) as follows:¹⁴

$$e_{ijk} = \frac{\partial P_i}{\partial \varepsilon_{jk}}, \quad (4)$$

$$d_{ijk} = \frac{\partial P_i}{\partial \sigma_{jk}}, \quad (5)$$

where sub-indexes $i, j, k \in \{1, 2, 3\}$ and 1, 2, and 3, respectively, correspond to Cartesian directions x , y , and z .

Besides the in-plane piezoelectric coefficients (e_{11}), the Janus ZrGeZ₃H monolayers also exhibit out-of-plane piezoelectric response (e_{31}) due to the lack of centrosymmetry. We use density functional perturbation theory to calculate the coefficients e_{ijk} by applying uniaxial deformation along the x -axis of orthorhombic supercell. We then evaluate the piezoelectric coefficients d_{ijk} through the following relationship:

$$d_{11} = \frac{e_{11}}{C_{11} - C_{12}}, \quad (6)$$

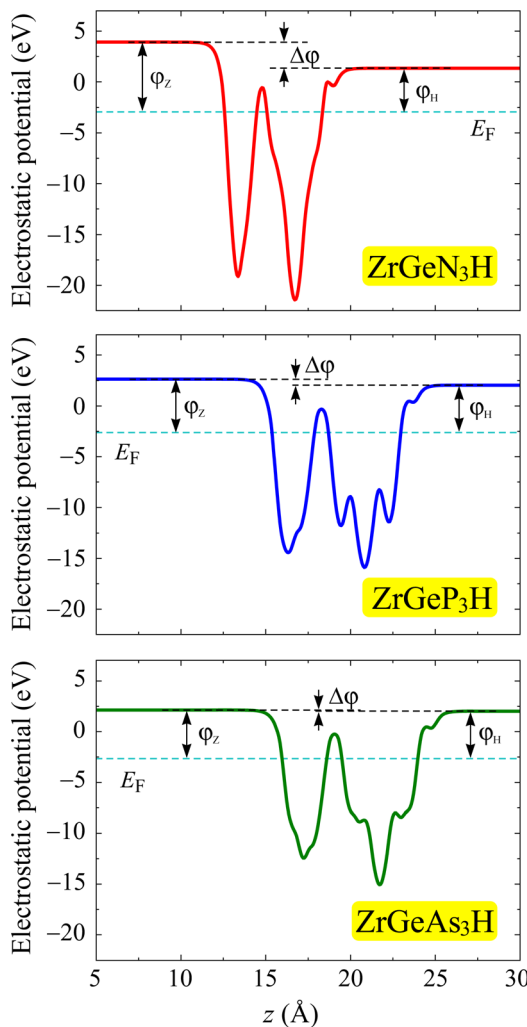


Fig. 6 Electrostatic potential of ZrGeZ₃H monolayers with the dipole correction. The dashed cyan line is set as the Fermi level.

Table 3 The PBE/HSE06 bandgap E_g (eV), vacuum level difference $\Delta\varphi$ (eV), and work function φ of ZrGeZ₃H monolayers

	E_g^{PBE}	E_g^{HSE06}	$\Delta\varphi$	φ_z	φ_H
ZrGeN ₃ H	1.99	3.28	2.59	6.86	4.27
ZrGeP ₃ H	0.48	1.15	0.58	5.26	4.68
ZrGeAs ₃ H	0.35	1.00	0.09	4.77	4.68

$$d_{31} = \frac{e_{31}}{C_{11} + C_{12}}. \quad (7)$$

Table 2 summarises the computed piezoelectric coefficients of the ZrGeZ₃H configurations. The piezoelectric coefficients e_{11} and d_{11} are 2.17×10^{-10} , -1.88×10^{-10} , -2.50×10^{-10} C m⁻¹ and 1.38 , -2.72 , -4.44 pm V⁻¹ for the ZrGeN₃H, ZrGeP₃H and ZrGeAs₃H systems, respectively. These results imply that the ZrGeAs₃H monolayer exhibits the highest piezoelectric response of all the proposed monolayers. The values of e_{11} and d_{11} are comparable to e_{11} and d_{11} obtained in MoGeN₃H³⁹ and

WSiZ₃H.⁴⁰ Additionally, the ZrGeZ₃H monolayers also possess the out-of-plane piezoelectric responses. The e_{31} coefficient reaches the highest value of 0.22×10^{-10} C m⁻¹ for the ZrGeN₃H monolayer, while the ZrGeAs₃H monolayer exhibits the highest magnitude d_{31} of -0.15 pm V⁻¹. The obtained e_{31} and d_{31} are similar to those reported in the Janus WSiZ₃H system.⁴⁰

3.4 Transport properties

At last, we study the mobility of carriers and related transport features of our Janus monolayers. The magnitude of the carrier mobility of 2D nanostructures is an essential factor for the nanoelectronics and optoelectronics. We can estimate the carrier mobility in 2D semiconductors based on the deformation potential (DP) method. According to this theory, the room temperature μ_{2D} of the three systems is determined by the following equation:

$$\mu_{2D} = \frac{e\hbar^3 C_{2D}}{k_B T m^* \bar{m} E_d}, \quad (8)$$

where m^* and $\bar{m} = \sqrt{m_x m_y}$ are the effective mass and average effective mass, respectively. T , e , \hbar , and k_B indicate, respectively, the temperature, the elementary charge, the reduced Planck constant, and the Boltzmann constant. E_d and C_{2D} are the deformation potential constant and elastic modulus, respectively. The effective masses of holes/electrons are defined as:

$$\frac{1}{m^*} = \frac{1}{\hbar^2} \left| \frac{\partial^2 E(k)}{\partial k^2} \right|, \quad (9)$$

Here $E(k)$ is the energy corresponding to wave vector k . Table 4 shows the effective mass achieved for the ZrGeZ₃H monolayers. The m^* values show the same trend in all three Janus systems. Taking the ZrGeN₃H system as an example, the effective mass of electrons and holes in the x direction is smaller than that in the y direction, and the electron mass is smaller than the hole mass along a given direction. This can significantly affect the mobility of carriers. The hole mass in the Janus ZrGeN₃H monolayer is the largest among the three monolayers, which is related to the electronic band structure as shown in Fig. 4.

Besides the effective mass, the deformation potential constant and elastic modulus also decide the value of carrier mobility, and they are expressed as follows:

$$C_{2D} = \frac{1}{Q_0} \frac{\partial^2 E_{\text{tot}}}{\partial \varepsilon_{\text{uni}}^2}, \quad (10)$$

$$E_d = \frac{\Delta E_{\text{edge}}}{\varepsilon_{\text{uni}}}, \quad (11)$$

where ΔE_{edge} is the shift of band-edge with respect to the vacuum level caused by the uniaxial strain. E_{tot} and Q_0 refer to the total energy and area of the supercell at equilibrium. Fig. 7 plots the energy shifting and band-edge positions as a function of the uniaxial strain along two transport directions. The achieved values of E_d and C_{2D} are shown in Table 4. We can realize that the ZrGeN₃H monolayer has larger $|E_d|$ and C_{2D} than the other monolayers.

Table 4 Effective mass of carriers m^* (in units of free electron mass m_0), 2D elastic modulus C_{2D} (Nm^{-1}), DP constants E_d (eV), and carrier mobility μ ($\text{cm}^2 \text{V}^{-1} \text{s}^{-1}$) of ZrGeZ_3H monolayers along the x and y axes

		m^*_x	m^*_y	C_{2D}^x	C_{2D}^y	E_d^x	E_d^y	μ_x	μ_y
Electron	ZrGeN_3H	0.26	0.30	140.59	140.59	-10.51	-10.50	369.81	320.17
	ZrGeP_3H	0.27	0.63	68.77	68.80	-1.99	-1.86	3408.37	1665.96
	ZrGeAs_3H	0.27	0.62	60.06	60.12	-1.80	-1.71	3639.20	1734.14
Hole	ZrGeN_3H	1.35	2.34	140.59	140.59	-5.78	-6.61	37.44	16.49
	ZrGeP_3H	0.87	1.08	68.77	68.80	-4.88	-4.98	72.53	56.20
	ZrGeAs_3H	0.81	0.95	60.06	60.12	-4.62	-4.72	84.34	68.96

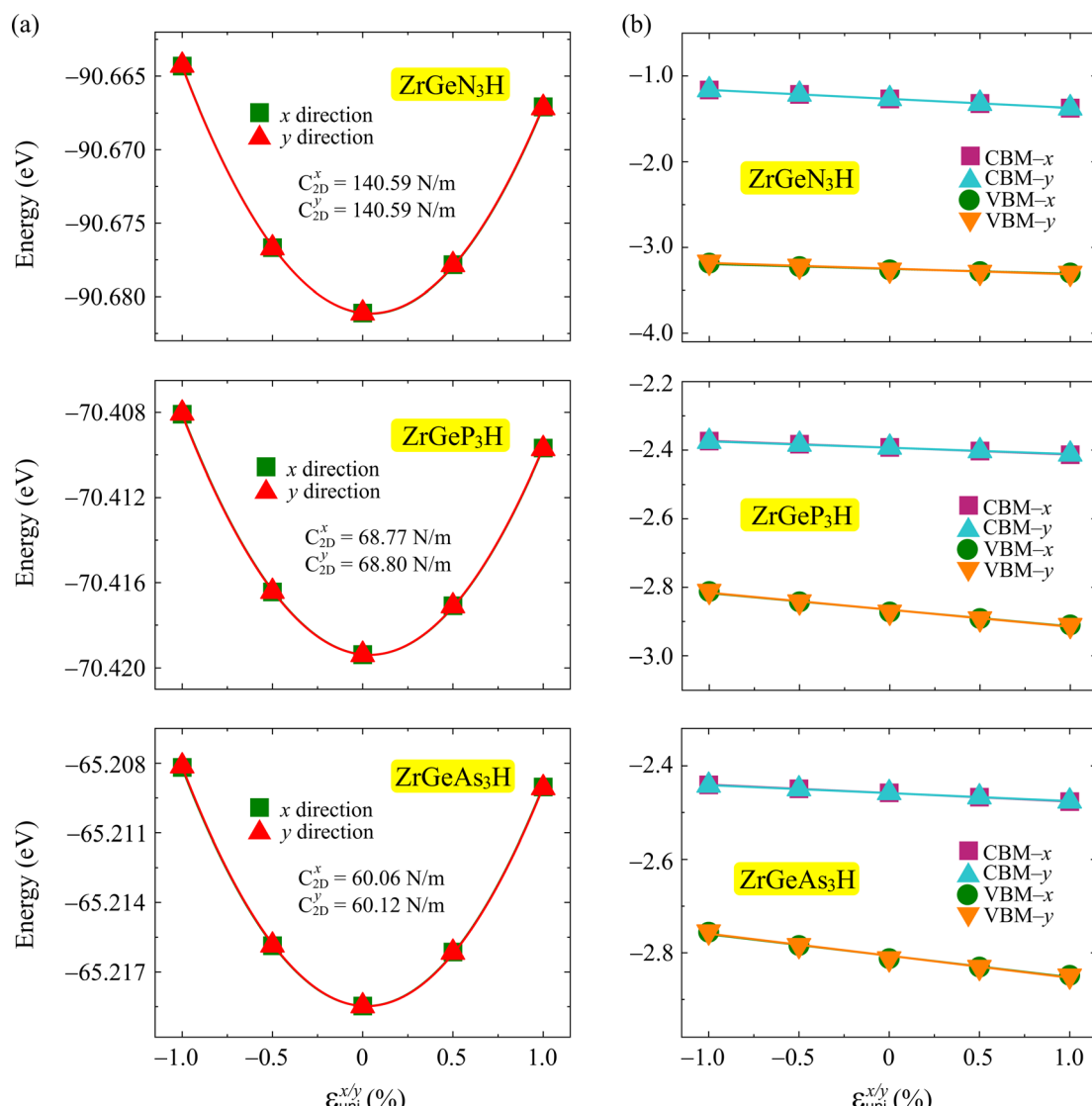


Fig. 7 The energy shifting (a) and band-edge positions as a function of the uniaxial strain of ZrGeZ_3H monolayers along x and y directions. The solid lines are the fitting curves.

Then we calculate the carrier mobility of three Janus ZrGeZ_3H monolayers based on the relevant parameters, and the calculated results are presented in Table 4. It can be seen that the electron mobility varies from 320.17 to 3639.20 $\text{cm}^2 \text{V}^{-1} \text{s}^{-1}$, while the hole mobility has a much smaller magnitude, from 16.49 to 84.34 $\text{cm}^2 \text{V}^{-1} \text{s}^{-1}$. Thus, there is a significant difference in the mobility

between electrons and holes in the given monolayers. The carrier mobility is also anisotropy in the different transport directions. The electron/hole mobilities exhibit different values along the two in-plane directions. As shown in Table 4, the ZrGeAs_3H and ZrGeP_3H monolayers have very high electron mobility of 3639.20 and 3408.37 $\text{cm}^2 \text{V}^{-1} \text{s}^{-1}$, respectively. Our calculated results



demonstrate that the ZrGeN_3H monolayer exhibits lower electron mobility than that in ZrGeAs_3H and ZrGeP_3H monolayers. This is due to the high value of the deformation potential constant (absolute value $|E_d|$) of ZrGeN_3H monolayer as listed in Table 4. The high $|E_d|$ of ZrGeN_3H suggests that the influence of uniaxial strains on its band-edge positions is significant. These values are one order of magnitude higher than the electron mobility in the conventional material MoS_2 .⁴¹ This suggests that our predicted monolayers have promising applications in electronic components.

4 Conclusion

To summarize, we have conducted a theoretical analysis based on the fundamentals of DFT calculations to explore the structural stability, electronic features, piezoelectricity, Raman response, and carrier mobility of the 2D Janus ZrGeZ_3H monolayers. The phonon dispersion spectra, AIMD simulation, cohesive energy, and elastic coefficient calculations confirm the structural stability of these systems. The computed band structures reveal that all proposed configurations are indirect semiconductors with band gaps ranging from 1.00 to 3.28 eV at the HSE06 level. For each Janus system, the work function at the H surface is smaller than at the Z surface. The obtained projected bands of the three ZrGeZ_3H systems indicate that the d orbital of the Zr element contributes mainly to the construction of the conduction band, while the p orbital of Z element has numerous participation in the formation of the valence band. Notably, we observe the coexistence of in-plane and out-of-plane piezoelectric coefficients in all three monolayers. In addition, the carrier mobilities of electrons and holes along transport directions are anisotropic. It is found that the electron mobility is high up to 3639.20 and 3408.37 $\text{cm}^2 \text{V}^{-1} \text{ s}^{-1}$ for ZrGeAs_3H and ZrGeP_3H systems, respectively. Our findings reveal that the 2D Janus ZrGeZ_3H structures are suitable candidates for piezoelectric and electric applications.

Data availability

The data that support the findings of this study are available upon reasonable request from the corresponding author.

Conflicts of interest

There are no conflicts of interest to declare.

Acknowledgements

This research is funded by Hue University under project number DHH2023-04-207. Khanh V Hoang acknowledges Phenikaa University for providing HPC computational resources.

References

- 1 J. Xin, Y. Zheng and E. Shi, *Appl. Phys. Lett.*, 2007, **91**, 112902.
- 2 M. N. Blonsky, H. L. Zhuang, A. K. Singh and R. G. Hennig, *ACS Nano*, 2015, **9**, 9885–9891.
- 3 Y. Chen, J. Liu, J. Yu, Y. Guo and Q. Sun, *Phys. Chem. Chem. Phys.*, 2019, **21**, 1207–1216.
- 4 M. Dragoman, A. Dinescu and D. Dragoman, *Phys. Status Solidi A*, 2019, **216**, 1800724.
- 5 Z. Liu, H. Wang, J. Sun, R. Sun, Z. F. Wang and J. Yang, *Nanoscale*, 2018, **10**, 16169–16177.
- 6 T. Tan, X. Jiang, C. Wang, B. Yao and H. Zhang, *Adv. Sci.*, 2020, **7**, 2000058.
- 7 F. R. Fan, R. Wang, H. Zhang and W. Wu, *Chem. Soc. Rev.*, 2021, **50**, 10983–11031.
- 8 Y. Zhu, L. Peng, Z. Fang, C. Yan, X. Zhang and G. Yu, *Adv. Mater.*, 2018, **30**, 1706347.
- 9 D. Li, Y. Gong, Y. Chen, J. Lin, Q. Khan, Y. Zhang, Y. Li, H. Zhang and H. Xie, *Nano-Micro Lett.*, 2020, **12**, year.
- 10 H. Zhu, Y. Wang, J. Xiao, M. Liu, S. Xiong, Z. J. Wong, Z. Ye, Y. Ye, X. Yin and X. Zhang, *Nat. Nanotechnol.*, 2014, **10**, 151–155.
- 11 C. Zhang, Y. Nie, S. Sanvito and A. Du, *Nano Lett.*, 2019, **19**, 1366–1370.
- 12 J. Zhang, S. Jia, I. Kholmanov, L. Dong, D. Er, W. Chen, H. Guo, Z. Jin, V. B. Shenoy, L. Shi and J. Lou, *ACS Nano*, 2017, **11**, 8192–8198.
- 13 L. Zhang, Z. Yang, T. Gong, R. Pan, H. Wang, Z. Guo, H. Zhang and X. Fu, *J. Mater. Chem. A*, 2020, **8**, 8813–8830.
- 14 K.-A. N. Duerloo, M. T. Ong and E. J. Reed, *J. Phys. Chem. Lett.*, 2012, **3**, 2871–2876.
- 15 W. Li and J. Li, *Nano Res.*, 2015, **8**, 3796–3802.
- 16 R. Fei, W. Li, J. Li and L. Yang, *Appl. Phys. Lett.*, 2015, **107**, 173104.
- 17 Y. Guo, S. Zhou, Y. Bai and J. Zhao, *Appl. Phys. Lett.*, 2017, **110**, 163102.
- 18 S.-D. Guo, X.-S. Guo, Z.-Y. Liu and Y.-N. Quan, *J. Appl. Phys.*, 2020, **127**, year.
- 19 M. Yagmurcukardes, C. Sevik and F. M. Peeters, *Phys. Rev. B*, 2019, **100**, 045415.
- 20 M. Yagmurcukardes and F. M. Peeters, *Phys. Rev. B*, 2020, **101**, 155205.
- 21 T. V. Vu, H. V. Phuc, A. I. Kartamyshev and N. N. Hieu, *Appl. Phys. Lett.*, 2023, **122**, 061601.
- 22 D. Bezzerga, E.-A. Haidar, C. Stampfl, A. Mir and M. Sahnoun, *Nanoscale Adv.*, 2023, **5**, 1425–1432.
- 23 Y.-L. Hong, Z. Liu, L. Wang, T. Zhou, W. Ma, C. Xu, S. Feng, L. Chen, M.-L. Chen, D.-M. Sun, X.-Q. Chen, H.-M. Cheng and W. Ren, *Science*, 2020, **369**, 670–674.
- 24 L. Wang, Y. Shi, M. Liu, A. Zhang, Y.-L. Hong, R. Li, Q. Gao, M. Chen, W. Ren, H.-M. Cheng, Y. Li and X.-Q. Chen, *Nat. Commun.*, 2021, **12**, 2361.
- 25 V. T. T. Vi, T. P. T. Linh, C. Q. Nguyen and N. N. Hieu, *Adv. Theory Simul.*, 2022, **5**, 2200499.
- 26 N. T. Hiep, N. P. Q. Anh, H. V. Phuc, C. Q. Nguyen, N. N. Hieu and V. T. T. Vi, *Phys. Chem. Chem. Phys.*, 2023, **25**, 8779–8788.
- 27 R. Sibatov, R. Meftakhtutdinov and A. Kochaev, *Appl. Surf. Sci.*, 2022, **585**, 152465.
- 28 G. Kresse and J. Furthmüller, *Phys. Rev. B: Condens. Matter Mater. Phys.*, 1996, **54**, 11169–11186.
- 29 G. Kresse and J. Furthmüller, *Comput. Mater. Sci.*, 1996, **6**, 15–50.



30 J. P. Perdew, K. Burke and M. Ernzerhof, *Phys. Rev. Lett.*, 1996, **77**, 3865.

31 J. Heyd, G. E. Scuseria and M. Ernzerhof, *J. Chem. Phys.*, 2003, **118**, 8207.

32 A. Togo, L. Chaput and I. Tanaka, *Phys. Rev. B*, 2015, **91**, 094306.

33 S. Grimme, J. Antony, S. Ehrlich and H. Krieg, *J. Chem. Phys.*, 2010, **132**, 154104.

34 M. Yagmurcukardes, F. M. Peeters and H. Sahin, *Phys. Rev. B*, 2018, **98**, 085431.

35 S. Nosé, *J. Chem. Phys.*, 1984, **81**, 511.

36 J. Bardeen and W. Shockley, *Phys. Rev.*, 1950, **80**, 72.

37 C. Lee, X. Wei, J. W. Kysar and J. Hone, *Science*, 2008, **321**, 385–388.

38 J. Kang, H. Sahin and F. M. Peeters, *Phys. Chem. Chem. Phys.*, 2015, **17**, 27742–27749.

39 X. Cai, G. Chen, R. Li, Z. Pan and Y. Jia, *J. Mater. Chem. C*, 2024, 4682.

40 T. V. Vu, B. D. Hoi, A. I. Kartamyshev and N. N. Hieu, *J. Appl. Phys.*, 2024, **135**, 074301.

41 B. Radisavljevic, A. Radenovic, J. Brivio, V. Giacometti and A. Kis, *Nat. Nanotechnol.*, 2011, **6**, 147–150.

